Palladium-based Ferroelectrics and Multiferroics: Theory and Experiment

Shalini Kumari[1], Dhiren K. Pradhan[1], Nora Ortega[1], Kallol Pradhan[1], Christopher DeVreugd[2], Gopalan Srinivasan[2], Ashok Kumar[3], Tula R. Paudel[4], Evgeny Y. Tsymbal[4], Alice M. Bumstead[5], J. F. Scott[5,*], and Ram S. Katiyar[1]

[1]Department of Physics and Institute for Functional Nanomaterials, University of Puerto Rico, San Juan, PR 00931, USA.
[2]Physics Department, Oakland University, Rochester, Michigan 48309-4401, USA.
[3]CSIR-National Physical Laboratory, Dr. K. S. Krishnan Marg, New Delhi 110012, India.
[4]Department of Physics, University of Nebraska, Lincoln, NE 68588-0299 USA.
[5]Department of Chemistry and Department of Physics, University of St. Andrews, St. Andrews KY16 ST, U. K.

Abstract

Palladium normally does not easily substitute for Ti or Zr in perovskite oxides. Moreover, Pd is not normally magnetic (but becomes ferromagnetic under applied uniaxial stress or electric fields). Despite these two great obstacles, we have succeeded in fabricating lead zirconate titanate with 30% Pd substitution. For 20:80 Zr:Ti the ceramics are generally single-phase perovskite (>99%), but sometimes exhibit 1% $PbPdO_2$, which is magnetic below T=90K. The resulting material is multiferroic (ferroelectric-ferromagnet) at room temperature. The processing is slightly unusual (>8 hrs in high-energy ball-milling in Zr balls), and the density functional theory provided shows that it occurs because of Pd^{+4} in the oversized Pb^{+2} site; if all Pd^{+4} were to go into the Ti^{+4} perovskite B-site, no magnetism would result.

*Author to whom correspondence to be addressed. Electronic mail: jfs4@st-andrews.ac.uk (J. F. Scott)

Introduction

The discovery and analysis of large room-temperature magnetoelectric effects in single-phase material are among the aims of scientists working worldwide in the area of multiferroics, similar to the desire for room-temperature superconductors. These systems require the presence of simultaneous ferroic order parameters with strong magnetoelectric (ME) coupling for an increased number of logic states. During the last fifteen years the multiferroic (MF) research communities have been searching for an alternative room temperature MF material beyond $BiFeO_3$ (which has high leakage current) with large ~~magnetoelectric~~ ME coupling for possible applications in high density electronic components, and low heat dissipation memory and logic devices.[1,2,3,4,5,6,7,8] In the past few years, we have investigated several multi-component systems such as $Pb(Zr,Ti)O_3(PZT)$-$Pb(Fe,Ta/Nb/W)O_3$, and related family members, which have shown better ME effects compared to bismuth ferrite.[9,10,11,12] In continuation to our search for larger ME effect, we have studied $Pb(Zr_{0.20}Ti_{0.80})_{0.70}Pd_{0.30}O_{3-\delta}$ (PZTP30) system with an unusually large (30%) palladium occupancy in the B-site of PZT. This material exhibited a ME coupling coefficient ~ 0.36 mV/cm.Oe [larger than most reported values for $BiFeO_3$ but about an order of magnitude lower than the highest reported (but unconfirmed) value of 7 mV/cm.Oe for nano-crystalline $BiFeO_3$].[13] This value is also an order of magnitude smaller than in cryogenic antiferromagnetic $LiCoPO_4$ or $TbPO_4$, or in ferromagnetic YIG (5.52, 6.62, and 5.41 mV/cm.Oe). For all $BiFeO_3$-based materials the highest known ambient value is for the $Bi_5Ti_3FeO_{15}$ compound ($\alpha_{ME} \sim 10$ mVcm^{-1} Oe^{-1}). In the case of $(BiFeO_3)_{1-x}$–$(BaTiO_3)_x$ and $Bi_{1-x}Nd_xFeO_3$ solid solutions, the maximum α_{ME} is of the order of 1 and 2.7 mVcm^{-1} Oe^{-1}; so our value is within an order of magnitude of that of the highest known ceramic.[14] Our new

system is a simple tetragonal crystal structure with space group *P4mm* as probed by X-ray diffraction (XRD) studies.

The basic aim of this paper is to discriminate between two possible explanations of detailed data on ceramic PZTP30: First, is it a single-phase ferroelectric perovskite with Pd^{+2} and Pd^{+4} substitutional at Pb A-sites and Ti B-sites respectively, and a room-temperature multiferroic; or second, is it merely a two-phase composite with ferroelectric PZT:Pd and a ferromagnetic second phase.

A neutral Pd atom (Kr $4d^{10}$) has square planar complex, which gives zero magnetic moment (μ=0) and diamagnetism, but when it is in Pd^{+2} or Pd^{+4} ionic states, it provides large magnetic moment with outer cell configuration $4d^8 5s^0$ or $4d^6 5s^0$ with unpaired electrons in its d-shell. Large electric fields can cause Pd to become ferromagnetic.[15,16,17,18] The presence of Pd in PZTP30 has been confirmed by XPS and XRF studies and assigned with related binding energies of Pd^{+2} and Pd^{+4} ions as 336.37 eV, 342.9 eV, and 337.53 eV, 343.43 eV, respectively, which may be the origin of room temperature magnetism in Pd substituted PZT ceramics. A sharp first order ferroelectric phase transition was observed at ~569 K (+/-5 K) for PZTP30, which is confirmed from dielectric, and thermal analysis. Both ferromagnetic and ferroelectric orderings with large ME are measured.

The basic physics and coupling mechanisms between spin and polarization in crystals, especially for single phase ME systems, is not well studied yet for the next generation of logic and memory elements.[19,20,21,22,23] Due to the natural chemical incompatibility between magnetism and ferroelectricity in oxide perovskites, only a few single-phase multiferroic oxides exist with sufficiently large magnitude of polarization and magnetization for real device applications. Some of the well-known potential multiferroic materials are as follows: $BiFeO_3$, $YMnO_3$,

$Pb(Fe_{0.5}Nb_{0.5})O_3$, $Pb(Fe_{0.5}Ta_{0.5})O_3$, $Pb(Fe_{0.67}W_{0.33})O_3$, $TbMnO_3$, etc.[8,12,24,25,26] The most well-known room-temperature lead-free single-phase multiferroic is $BiFeO_3$ (BFO), having both ferroelectric ($T_C = 1143$ K) and antiferromagnetic ($T_N = 643$ K) phase transitions above room temperature; however, still it is not suitable for real practical device applications due to high leakage current and small ME coupling coefficient.[27,28,29,30] Multiferroics possess ferroic order parameters and cross coupling at cryogenic temperatures (either ferroelectric and/or magnetic transitions); among these the magnitude and directions of magnetic and ferroelectric orders often occur largely independent of each other; and as a result, the magnetoelectric coupling tends to be small.[31,32,33] The low operational temperatures (ferroelectric/magnetic), high leakage current, and/or weak ME coupling of most of the single-phase compounds have motivated researchers to continue the search of novel room temperature magnetoelectric multiferroics with larger ME coupling coefficients.

An alternate option is ferroelectric and ferromagnetic composites/heterostructures which have greater design flexibility for ME devices by combining ferroelectric (FE) and ferromagnetic (FM) phases together; among them a heterostructure with FE/FM phases is the most popular design, due to immense potential for high density logic states.[34] Single-phase magnetoelectric materials with large ME coupling coefficients in ultrathin hetero-structured films are important for tunnel junction-based devices, which can provide a higher degree of logic states under combined electric and magnetic control. These factors drive the endeavors for discovering new room temperature single-phase multiferroics with giant ME coupling, beyond $BiFeO_3$. Several materials have recently been discovered, such as $Pb(Zr_{0.53}Ti_{0.47})_{0.60}$ $(Fe_{0.5}Ta_{0.5})_{0.40}O_3$ (PZTFT), and the Bi-based Aurivillius oxides, $GaFeO_3$, and $LuFeO_3$.[9,35,36,37,38,39]

Therefore, the discovery of an alternative room temperature single phase multiferroic material is exciting. In this report an attempt has been made to realize multiferroism and ME coupling at room temperature in $PbZr_xTi_{1-x}O_3$, which is known to be one of the best ferroelectric materials in nature, whereas palladium is a transition metal usually without any magnetic properties.[40,41] However, we have found multiferroicity (ferroelectricity and magnetism) with strong intrinsic ME coupling at room temperature in the palladium-substituted PZT.

Experimental Details

Polycrystalline powder of $Pb(Zr_{0.20}Ti_{0.80})_{0.70}Pd_{0.30}O_{3-\delta}$ (PZTP30) were synthesized using a conventional solid-state reaction route from a stoichiometric mixture of highly pure (>99.99%) reagents PbO, ZrO_2, TiO_2, and PdO powders from Alfa Aesar. Mechanical ball milling of stoichiometric amounts of all ingredients was carried out in methanol with Zr balls (to avoid magnetic contamination), followed by calcination in air at 1150 ^{o}C for 8h, using a carbolite furnace (HTF1700) with heating rate of 5°C/min. This is a rather long time for a high-energy, high-temperature ball milling, and we believe that significant solid state chemistry occurred during the milling [ref. Materials Letters 39 1999 364–369; Mechanochemical synthesis of nanosized lead titanate powders from mixed oxides; Junmin Xue, Dongmei Wan, John Wang).]. The synthesized phase-pure powder was pressed into pellets (d=13 mm) at a uniaxial force of 5 tons and later sintered at 1200 ^{o}C for 8h. Phase formations of the pellets were evaluated by X-ray diffractometer (Rigaku Ultima III) equipped with a CuK_α radiation source operating in the Bragg–Brentano geometry at 40 kV and 40 mA in a slow-scan mode 0.2^o/min. The Rietveld structure refinement was carried out using FullProf Suite Software. Scanning electron microscopy (SEM) images were recorded at 5000X magnification with help of a JEOL JSM-6480LV system operated with an accelerating voltage of 20 kV to study the surface morphology.

The composition and valence states of the fabricated pellets were confirmed via X-ray fluorescence spectroscopy (XRF), Energy-dispersive X-ray spectroscopy (EDS), and high-resolution X-ray photoemission spectroscopy (XPS), correspondingly. The flat surface of the sintered pellets was polished with fine emery paper, and then top and bottom electrodes were made by coating high purity silver paint followed by heating at 200 $^{\circ}$C for 2 h in air for better conduction and adhesion. The dielectric measurements were performed under vacuum (10^{-6} Torr) using an HP4294A impedance analyzer. Thermal control was achieved in the range of 200 – 700 K using a variable temperature micro-probe system equipped with a programmable temperature controller (MMR Technologies, Inc.). Ferroelectric properties were measured using Radiant RT 6000 High Voltage System after poling the sample under a voltage of 1000 V for 6 h using DC Power supply (TREK, Inc., Model: 677A) at room temperature. Low temperature magnetic properties of the PZTP30 samples were measured using a Quantum Design PPMS DynaCool in a wide range of temperature 25-300 K. The room temperature magnetoelectric measurements were carried out with a homemade ME-set up using a magnet with varying field of up to $\pm$3kOe with lock-in amplifier and reference ac magnetic field, using a Helmholtz coil. [42]

Results and Discussion

Structural, Microstructural and Elemental Characterization

The Rietveld refinement of high resolution XRD data provides straightforward and precise structural information. Detailed XRD studies have been performed on PZTP30 pellets used for magnetic, and ME measurements with assumption of A-site occupancy by Pb and B-site by Zr, Ti, and Pd with oxygen at the corner of BO_6 octahedral position. The Rietveld refinement of the diffraction patterns was performed by considering tetragonal *P4mm* symmetry.[43,44] The

experimental and Rietveld simulated XRD patterns of PZTP30 bulk samples are shown in Figure 1(a). The results demonstrated excellent fit, confirming pure tetragonal phase formation of the material belonging to the space group *P4mm.* The sharp Bragg peaks were assigned to their Miller indices with only a single very weak appearance of an extra reflection peaks that would be indicative of secondary phases and no peaks from lead-deficient pyrochlore phases. In particular, we do find PdO, which is magnetic at room temperature, but in amounts <1%, as shown by the XRD reflection at 34.2° in Figure 1(b).[45,46,47] The XRD are also known now for $PbPdO_2$, another magnetic palladium oxide at low temperatures (T < 90K), and although these are coincidentally hidden under the strongest PZT XRD lines, we find them at the 1% level in pure $PbTiO_3$:Pd. We refined many parameters, such as background, zero shift, specimen displacement, atomic positions, thermal factors, scale factor, lattice parameters, FWHM, and shape parameters. Pseudo–Voigt description of profile shape was taken into account as a profile set-up for Rietveld refinement. The difference between the measured spectrum and the refined one is very small, and the reliability is ensured by the refinement parameters. All atoms were fixed to their site occupancies, as their variation did not appreciably affect the refinement results. During the refinement process it was observed that reliability factors improve further when anisotropic thermal parameters were taken into account compared with the isotropic thermal parameters of the individual atoms. The crystal structure parameters, and reliability factors obtained after XRD refinement are listed in Table S1 and S2 match well with the reported values for $Pb(Zr_{0.20}Ti_{0.80})O_3$.[43] The calculated tetragonality ratio was c/a = 1.047, which indicates a preference for large polarization. Using the obtained unit cell parameters and atomic positions, a three-dimensional sketch of tetragonal PZTP30 unit cell projected along c axis has been simulated, as shown in Figure 1(c), which indicates that Pd was incorporated into the crystalline

lattice of the PZT; hence the appearance of tetragonality in PZTP30 is consistent with PZT(20/80), the highly tetragonal Ti-rich version of PZT.[43,44,48,49] The bond lengths obtained after XRD refinement have been compiled in Table S3.

In any study of new multiferroics it is essential to demonstrate that the magnetic and ferroelectric properties arise from a single chemical phase, and that it is not a situation in which ferromagnetism originates from a second phase. To this end we have examined carefully via SEM the ceramic materials in this study. The overall microstructure of PZTP30 pellets showed well-defined densely packed grains with average size ranging between $\sim 3-10\,\mu$m surrounded by distinct grain boundaries, as shown in Figure 2(a). The presence of different shapes and grain sizes with neck-to-neck compaction revealed that the grain growth process was almost completed during the sintering process. The Zr:Ti 20:80 specimens were mostly single-phase terraced perovskite (Figure 2(b)); however, for Zr:Ti near 50:50 several phases were observed. For the latter the electron micrographs reveal three distinct grain structures: The largest in percentage and grain size have pseudo-hexagonal habitats; the second largest are rectilinear tetragonal; and there is a small percentage of a third phase (plus traces of Al, due to sintering in an alumina crucible). However, PdO in nano-phase is ferromagnetic above room temperature, and $PbPdO_2$ is also ferromagnetic only below T=90K.[45-48] Since both are tetragonal, they are viable candidates for our tetragonal grains in the SEM micrographs of the 50:50 Ti/Zr specimens. This is discussed further below. However, even without examination of the SEM data, we note that most of the Pd is Pd^{+4}, whereas the only two room-temperature magnetic phases anticipated as possible contaminants in this composite are PdO and $PbPdO_2$, both of which are purely Pd^{+2}. PdO is weakly observed in the XRD data at $2\theta = 34.2^o$, but at <1% by weight. No XRD lines corresponding to the known diffraction pattern of $PbPdO_2$ are observed. The SEM data in Figure

2 support our view that the 20:80 PZT is primarily (99%) single-phase perovskite. In a separate paper (E. Graudauskaite et al.) we will present detailed studies of a second phase, identified as $PbPdO_2$, which is magnetic below T=90K; in PZT the XRD Bragg peaks happen to occur directly under those vfrom PZT, so they are not visible in the present work. We measure the atomic %, magnetic properties, and TEM of $PbPdO_2$ in that paper.

TEM data:

Some TEM data were also obtained. These have better resolution than the SEM and permit atomic percentages for individual grains. These will be discussed further in a separate paper but support the conclusions here.

The presence of all elements in PZTP30 bulk was confirmed through XRF measurement. The Table S4 gives the percentage (%) of the actual molar mass and molar mass obtained from XRF analysis of all individual elements in PZTP30 bulk. The average XRF data matched with the initial elemental compositions taken for this study within the experimental limitations as shown in Table S4. The EDX data confirm that the ratio of Pd/Pb was generally somewhat higher than the intended 30%; this may arise from surface excess or from our theoretically based hypothesis that Pd goes into both the Ti^{+4} sites and the Pb^{+2} sites.

For conclusive evidence of existence of all elements with their valence states, PZTP30 pellets were examined by high-resolution X-ray photoelectron spectroscopy (XPS). Figures 3 and S6 show the core level high resolution XPS spectra of Pb 4f, Zr 3d, Ti 2p, Pd 3$d,$ and O 1s. The peak positions in the XPS spectra were referenced to C 1s peak at 284.8 eV. The observed binding energy positions of Pb are Pb 4$f_{7/2}$ =138.2 eV, and Pb 4$f_{5/2}$ = 143 eV respectively. The high resolution XPS spectrum of Zr 3d, and Ti 2p splits up into two components due to spin-orbit

coupling. The spin-orbit doublets of Zr, and Ti were observed at following binding energies: Zr $3d_{5/2}$ = 181.3 eV, and Zr $3d_{3/2}$ = 183.7 eV; Ti $2p_{3/2}$ = 457.8 eV, and Ti $2p_{1/2}$ = 463.5 eV. These energy values confirm the valence states of Zr^{4+}, and Ti^{4+} ions without any trace of Ti^{3+} ions (which could in principle be responsible for some magnetism). Note that Pd^{4+} is an excellent fit in the B-site since it and sixfold-coordinated Ti^{4+} have the same (0.061-0.062 nm) ionic radii. Pd^{2+} is too small to fit well in the Pb^{2+} site. The Pd $3d_{5/2}$ and Pd $3d_{3/2}$ doublets were deconvoluted into Pd^{2+} at binding energy 336.37 eV, 342.9 eV, and Pd^{4+} at binding energy 337.53 eV, 343.43 eV respectively in PZTP30 ceramics (see Figure 3(a)).[50] The integrated intensity (occupied by Pd^{4+} ions) is quite large compared to Pd^{2+} ions (ratio: 4/3), which is the origin of magnetism in Pd-substituted PZT ceramics. The O1s can be deconvoluted into two peaks with binding energies of 531.1 eV and 529.3 eV with shallower binding energy peak belonging to the lattice oxygen and the deeper binding energy attributed to the surface adsorbed oxygen (see Figure 3(b).[51] The binding energies for all the individual elements match the standard value.[52] Moreover, the presence of all elements in PZTP30 bulk was confirmed clearly through XPS measurement along with XRF measurement.

Dielectric, and Thermal Studies

Temperature and frequency dependent dielectric studies were carried out over a wide range of temperatures and frequencies to understand the ferroelectric to paraelectric phase transition behavior, and dielectric dispersion characteristic. The order and nature of the phase transition allows us to understand the domain dynamics above and below the Curie temperature (T_c). The variation of relative dielectric permittivity (ε_r) and loss tangent (tan δ) as a function of temperature at different frequencies for PZTP30 is shown in Figure 4(a) and its inset, respectively. The dielectric permittivity decreases with increase in frequency for PZTP30, which

is a signature of polar dielectrics. Here ε_r increases with increase in temperature, reaches a maximum, and then decreases. This observed sharp anomaly at ~569 K (+/- 5K) represents the ferroelectric-paraelectric transition temperature (T_C). This further increases above ~600 K due to thermally activated charge carriers. (Note that T_c for undoped PZT at this 20:80 Zr/Ti ratio is ca. 720K.) The temperature dependent tan δ (inset of Figure 4(a)) also shows an anomaly just below T_c above 1 kHz probe frequencies. At high temperatures the value of tan δ increases with rise in temperature, which may be due to space charge polarization, and interfacial polarization across the Ag/PZTP30 interface. The substitution of Pd in PZT shifts the phase transition towards lower temperature. The observed T_c was further verified by differential scanning calorimetric (DSC) measurements as shown in Figure 4(b). The DSC curve indicates a sharp exothermic peak around 552 K (+/- 5K) corresponding to ferroelectric-paraelectric phase transition temperature. The temperature for an exothermic peak in DSC thermogram is nearly same as the ferroelectric phase transition temperature obtained from dielectric studies within the experimental uncertainty.

Ferroelectric and Magnetic properties

For the conclusive evidence of existence of ferroelectricity at room temperature, electrical polarization (P) versus electric field (E) hysteresis loop measurements have been carried out on PZTP30 samples at room temperature and shown in Figure 5(a). The P-E hysteresis loop measurements were performed on a poled ceramic sample. The coercive field (E_c), remanent polarization (P_r) and saturation polarization (P_s) are found to be 6.5 kV/cm, 10 μC/cm^2, and 16 μC/cm^2 respectively with the maximum applied electric field (20 kV/cm). The presence of a saturated ferroelectric hysteresis loop confirms the presence of ferroelectric properties in Pd substituted PZT ceramics.

11

Electrical hysteresis loops of PZTP30 ceramics were also measured using the Positive-Up Negative-Down (PUND) method before and after poling, to determine the accurate remanent ferroelectric polarization (P_r). PUND data provide, switchable polarization (dP) ~ 6 $\mu C/cm^2$ and switchable remanent polarization (dP_r) ~ 5 $\mu C/cm^2$ respectively as shown in Figure 5(b), where the net switchable polarization (dP) is as follows:

dP = P^* - $P^\wedge$, where P^* = (switchable polarization + non-switchable polarization) and $P^\wedge$ = (non-switchable polarization);

dP_r = P^*_r - $P^\wedge_r$, where P^*_r = (switchable remanent polarization + non-switchable remanent polarization) and $P^\wedge_r$ = (non-switchable remanent polarization).

The PUND data shown are not for the same specimen that was used for the hysteresis curve in Fig.5a but for a leakier sample to show that even in that case the hysteresis is real ferroelectricity and not charge injection.

In order to prove the presence of magnetism, and to understand the origin of magnetism in PZTP30, magnetization as a function of magnetic field at room temperature is depicted in Figure 5(c). Figures S7(a-d) show the M(H) hysteresis behavior performed at various temperatures. Standard PZT pellets were synthesized in same conditions as standards and do not show any magnetic ordering, whereas the Pd-doped PZT shows room-temperature well saturated M-H curves with a large tail due to diamagnetic properties for higher applied magnetic field. Temperature-dependence of coercive field (H_c) and remanent magnetization (M_r) of PZTP30 is shown in lower inset of Figure 5(c), which monotonically increases with decrease in temperature. In work to be published separately we see a distinct drop in M(T) at T=90K, where a second phase (1% $PbPdO_2$) exhibits its ferromagnetic-paramagnetic transition. Since no

impurity phase at >1% level has been detected in the XRD patterns of PZTP30, the observed room-temperature magnetism could be due to the presence of Pd^{2+}/Pd^{4+} ions into the PZT host lattice, leading to the emergence of ferromagnetic long-range ordering. Room-temperature ferromagnetism in some perovskite oxides have already been reported by substitution of ferromagnetic particles such as Ni, Fe, and Co into the host lattice.[53,54] The presence of Pd^{2+} and Pd^{4+} states in PZTP30 is viewed by us as the origin of magnetism, and the existence of Pd^{2+} and Pd^{4+} states has been already confirmed from the XPS and XRF studies (Figures 3 and S4). The zero-field-cooled (ZFC) and field-cooled (FC) behavior of PZTP30 at 500 and 1000 Oe from 25 to 300 K has been plotted in Figures S7(e) and 5(d) respectively**.** ZFC/FC data confirmed that there is no sharp transition up to 300 K. The results above prove that both ferroelectric and ferromagnetic ordering exists above room temperature and hence room temperature multiferroic properties.

Magnetoelectric Properties

For further understanding of the multiferroic nature, and the coupling between electric and magnetic order parameters in PZTP30 was investigated by studying the sample response to applied magnetic fields. The low-frequency magnetoelectric (ME) voltage coefficients (α_{ME}) were measured. The sample was first poled at room temperature in an electric field of 30 kV/cm for 4 hours. The ME measurement system consisted of an electromagnet for applying a bias magnetic field H, a pair of Helmholtz coils for applying an ac magnetic field δH, and lock-in detection for measuring the ME voltage δV generated across the sample thickness. The ME voltage was measured as a function of H for H = 0-3 kOe, an ac field δH = 1 Oe at 100 Hz and at room temperature. The measurements were performed for two field orientations: first in-plane mode for H and δH parallel to each other and to the sample plane (along direction *1)* and

perpendicular to δE along direction *3* (termed transverse orientation); and second, out-of-plane

mode for all the three fields (H, δH, and δE) parallel to each other and perpendicular to sample

plane (all the fields along direction *3* and termed longitudinal orientation).[42] The ME voltage

coefficient $\alpha = \delta V/(t \, \delta H)$ where t is the sample thickness was estimated. The H dependence of

longitudinal (α_{33}) and transverse (α_{31}) coupling coefficient for PZTP30 is plotted in Figure 6.

Figure 6 shows representative data on bias magnetic field (H) dependence of

transverse and longitudinal ME voltage coefficients. Consider first the results for the

longitudinal field direction ($\alpha_{E,33}$). As H is increased, $\alpha_{E,33}$ remains small for H < 0.7 kOe

and then there is an increase in $\alpha_{E,33}$ with H to a maximum value of 0.36 mV/cm Oe at H_m=

3 kOe. Upon reversal the direction of H, there is a sign reversal in $\alpha_{E,33}$ (a phase shift of

180°). The magnitude of $\alpha_{E,33}$ is small compared to values for positive fields and reaches a

maximum of 0.18 mV/cm Oe, which is only 50% of the value for +H. This asymmetry in

ME coefficient could be due to a magnetic anisotropy in the sample. The ME voltage

coefficient versus H data do not show a peak or decrease to zero value for very high H due

to saturation of magnetostriction. Similar observations were reported for several multiferroic

composites.[55,56,57,58]

Figure 6 also shows α vs. H data for field perpendicular to the sample plane. The ME

coefficient $\alpha_{E,31}$ shows a sign reversal relative to $\alpha_{E,33}$ and its magnitude increases almost

linearly with H to a value of 0.15 mV/cm Oe. Upon reversal of direction of H, $\alpha_{E,31}$ becomes

positive and shows a maximum value of 0.3 mV/cm.Oe, which is twice the magnitude for

+H. Since the ME voltage arises due to magnetic-mechanical-electrical interactions, the

voltage coefficients are directly proportional to the product of piezoelectric (*d*) and

piezomagnetic (q) coupling factors.[57,58,59] Since the parameter $q=d\lambda/dH$, where λ is the magnetostriction, the H-dependence of α is expected to track the slope of λ vs. H. Saturation of λ at high field leads to $\alpha_E = 0$. In this particular system, however, the data in Figure 6 clearly indicate that saturation of λ does not happen for H = 3 kOe. For most ferromagnets, the longitudinal (λ_L) and transverse (λ_T) magnetostrictions follow the relation $\lambda_L=2\,\lambda_T$ and one expects $\alpha_{33}=2\,\alpha_{E,31}$. For the data in Figure 6, one estimates for H = 3 kOe $\alpha_{33} \sim 2\,\alpha_{E,31}$ for +H and $\alpha_{31} \sim 2\,\alpha_{E,33}$ for –H.

In the case of a bulk composite in which the magnetostrictive and the piezoelectric phases are uniformly mixed together, the transverse ME signal is formed by transverse magnetostriction whereas the longitudinal ME signal is due to the longitudinal magnetostriction. For a majority of ferromagnets the longitudinal magnetostriction is a factor of two higher than the transverse magnetostriction, and one expects $\alpha_L = 2\,\alpha_T$. Such an empirical relationship is confirmed in samples in the shape of cubes.[59] To measure both coefficients and to avoid the influence of demagnetizing fields, it is necessary to use long cylindrical samples. But such an approach also leads to other difficulties: high voltage required for polarization and mismatch of input impedance of the measuring device with the impedance of the sample. One possible solution is to measure $\alpha_{E,T}$ for a disk sample of a bulk composite and then estimate the longitudinal coefficient from the empirical relationship.

Theory

To understand the microscopic origin of magnetism in Pd doped $Pb(Zr,Ti)O_3$, we consider a Pd-doped $PbTiO_3$ (PTO) as a model system. Similar to the $Pb(Zr,Ti)O_3$, PTO is non-magnetic and

can be expected to have similar electronic structure. To test if the isolated doping of PTO by Pd results in appearance of a magnetic moment in the system, we consider a 2x2x2 supercell of PTO where a Pd atom substitutes either Pb or Ti atom (see insets in Figure 7). Figures 7(a) and 7(c) show the total density states (DOS) of the Pd doped PTO (red curves) when PD atoms substitutes Pb or Ti atoms respectively, in comparison to the DOS of the bulk PTO (grey background in Figures 7(a) and 7(c)). Figure 7(b) and 7(d) shows the density of states (DOS) projected to Pd atom on Pb (Ti) site. It is evident that in both cases the induced defect states lie in the conduction and valence bands with no occupied defect states in the band gap of PTO. This indicates that Pd on Pb (Ti) site behaves as an isoelectronic substitution and the system remains insulating and non-magnetic.

Next, we consider doping PbTiO$_3$ with a large concentration of Pd as in the experiment. To model this, we replace two Ti or Pb cations that are first or second nearest neighbors with Pd in the 2x2x2 cubic supercell. Out of many ways to distributing two Pd atoms in the supercell, only when Pd replaces nearby Ti and Pb atoms along the [111] direction, as shown in Figure 8(d), the magnetic moment of ~ 2 µB appears in Pd replacing Pb. Figure 8(a) shows DOS of the defective system containing Pd in nearby Ti and Pb site compared to non-defective bulk system. In contrast to the isolated Pd substitution in Pb and Ti site (Figure 7(a) and Figure 1(c)) the defect states appear in the band gap of the bulk PTO. Figure 8(b) shows DOS projected to the Pd replacing Pb atom reveals spin split band, that arises from the exchange splitting of a DOS peak at ~2.0 eV (Figure 7(d)). The exchange split majority band holds approximately one additional electron resulting in a magnetic moment of ~1 µB/Pd. The remaining ~ 1µB comes from spin polarization of the DOS of the oxygen atoms bonded to Pd replacing Pb. In contrast density of states projected to the Pd replacing Ti (Figure 8(c)) atom shows almost no spin-polarization. The

two electrons in spin majority bands can be thought as donated by nominally 4+ Pd atom residing on nominally 2+ Pb atom producing magnetism.

The splitting of the defect band of Pd on Pb site can be understood in terms of the Stoner model[60]. In Figure 8(e), we compare density of states of the doped Pd on Pb site in PTO with the bulk Pd and found that paramagnetic density of state of Pd at Pb site enhanced by ~65%. As a result, the stoner criterion— $ID(E_F) > 1$, where I is a Stoner exchange parameter— satisfies and favor magnetic states.

Energetically, isolated replacement of Pd on Pb site is more favorable compared to the Pd doping Ti atoms. The calculated formation energy $\Delta H(D) = E(D) - E(\text{Clean}) + \mu_r - \mu_a$, where $E(D)$, $E(clean)$ are energy of defective and clean system, μ_r and μ_a are the energy of removed and added atoms) of the Pd replacing Pb atom (~2.5 eV) is much smaller than that (~8.7 eV) of Pd replacing Ti atoms. The difference between Pd replacing Pb and Ti site is so large that the conversed results from the larger cells would not change qualitative conclusions, whenever atomic energy sometime referred as chemical potentials remain the same. Additionally, we also calculated the defect pair binding energy,

$$\Delta E = \Delta H(\text{Defect pair}) - \Sigma \Delta H(\text{Individual defect}),$$

and found that when nearby Pb and Ti along [110] direction are replaced by Pd, the binding energy is negative ($\Delta E \sim -0.2\ eV$). However, such solutions are unfortunately non-magnetic. The magnetic solutions we found have positive binding energy ($\Delta E = \sim 1.0\ eV$). This indicate that that the possibility of forming such pair and having magnetic solution is very small even when doped with large concentration of Pd, consistent with small magnetic signal found experimentally.

Computational Methods

The theoretical modeling was performed using density functional theory (DFT) within the projected augmented wave (PAW) method for the electron- ion potential[61] and the local density approximation (LDA) for exchange and correlation, as implemented in Vienna *ab initio* simulation package (VASP)[62,63] The calculations were carried out using kinetic energy cutoff of 340 eV and 6×6×6 k-point mesh for Brillouin zone integration. We fully relaxed ionic coordinates with the force convergence limit of 0.001 eV/atom. We used theoretical LDA lattice constant of ferroelectric PbTiO3 for the calculations. The methods beyond LDA generally include Coulomb interactions that increases the host band gap and splitting of defect states. Each of these effect likely to enhances magnetism.   Separate calculations including modest U=3.0 eV yielded a similar result. For all Pd+4 at Ti+4 perovskite B-sites we find no magnetism. But for some Pd^{+4} at Pb^{+2} sites, the system is predicted to be a room-temperature ferromagnet. In the latter calculation the source of valence compensation is not explicitly given; but we assume that the Pd^{+4} at the Pb-site is balanced by Pd^{+2} at the Ti^{+4} B-site. Parenthetically we note that a similar hypothesis has been made for our recent data on ferroelectric $SnTiO_3$, where a relaxor behavior is found and attributed to be due to Sn^{+4} at the A-site and Sn^{+2} at the Ti B-site.[64]

Conclusions

A novel single phase-pure PZTP30 magnetoelectric having tetragonal crystal structure with *P4mm* symmetry was discovered for possible room temperature multi-states tunable logic and nonvolatile memory elements under external E and H-fields. It possesses high magneto-electric coefficients ~0.36 mV/cm.Oe at H_m= 3 kOe in a single-phase system suggesting a strong coupling between piezo- and magneto-striction at nanoscale. It displays room-temperature weak ferromagnetism, strong ferroelectricity, and strong ME coupling. We believe the origin of

magnetism is due to mixed valence states of the Pd^{2+}/Pd^{4+} in PZT matrix, and in particular the presence of Pd^{+4} at Pb^{+2} perovskite A-sites, as confirmed by XPS and XRF studies experimentally and DFT models. A sharp ferroelectric-paraelectric phase transition is observed near T = 569 K, well supported by dielectric, and thermal studies. The giant room-temperature magneto-electric coupling makes it a possible future alternative of $BiFeO_3$ with a strong possibility for real device applications. PdO and possibly $PbPdO_2$ are magnetic contaminant phases in our ceramic samples, but only at cryogenic temperatures and are measured as <1% abundance. $PbPd_2O_4$ is also magnetic, with a monoclinic-tetragonal I2/a to $I4_1$/a transition at T=240 K,[65] but it is metallic and centric and hence cannot contribute to ferroelectricity or magnetoelectricity; we do not find it in our samples.

Acknowledgement

Figure Captions

Figure 1. (a) The Rietveld refined XRD patterns of PZTP30 ceramics using Fullprof Suite Software; note the weak line due to <1% PdO; (c) The three-dimensional schematic sketch of the PZTP30 unit cell with tetragonal structure at room temperature.

Figure 2. SEM micrograph of PZTP30 ceramic with 20:80% Zr/Ti, showing single-phase perovskite structure with terraced grains.

Figure 3. (a) XPS spectra of Pd $3d$ deconvoluted into two peaks, the binding energies at 336.37 eV, 342.9 eV, and 337.53 eV, 343.43 eV are assigned to Pd^{2+} and Pd^{4+} respectively, (b) XPS spectra of O in PZTP30 ceramics at room temperature.

Figure 4. (a) Temperature dependence of relative dielectric constant of PZTP30 ceramics at different frequencies, the inset shows respective temperature dependence of tanδ, (b) DSC thermogram of PZTP30 ceramics.

Figure 5. (a) Ferroelectric (P-E) hysteresis loops of PZTP30 at room temperature; (c) Magnetic (M-H) hysteresis loops of PZTP30 at room temperature, M-H hysteresis loops of PZTP30 at 25 K (upper) and temperature dependence of H_c and M_r (lower) are in insets, (d) ZFC and FC plot of PZTP30 ceramics at 1000 Oe.

Figure 6. Magnetoelectric coupling coefficients (α_{E33} and α_{E31}) of PZTP30 ceramics as a function of an externally applied magnetic field H at room temperature.

Figure 7. Comparison between total density of states (DOS) of defective (shown in red) with (a) Pd replacing one Pb and (c) Pd replacing Ti, and clean $PbTiO_3$ (shown as a gray background). The DOS states projected to the Pd atom replacing Ti (b) and Pb (d). The structure shown in (b) and (d) was used for the calculations. In both cases there are no defect states in the gap and overall the system remains non-magnetic and insulating. In (d) the states at ca. 2 eV above the Fermi level are Pd d-states of e sub-g symmetry.

Figure 8. Comparison between majority (positive) and minority (negative) density of states (DOS) of the two Pd doped defective, shown in red, and clean bulk $PbTiO_3$. The m (a). Projected density of states to the Pd site replacing Pb site (b), Ti site (c). The former shows significant spin polarization. The structure of defective system (d) and the paramagnetic density of state of Pd on Pb site in PTO compared with that of bulk Pd.
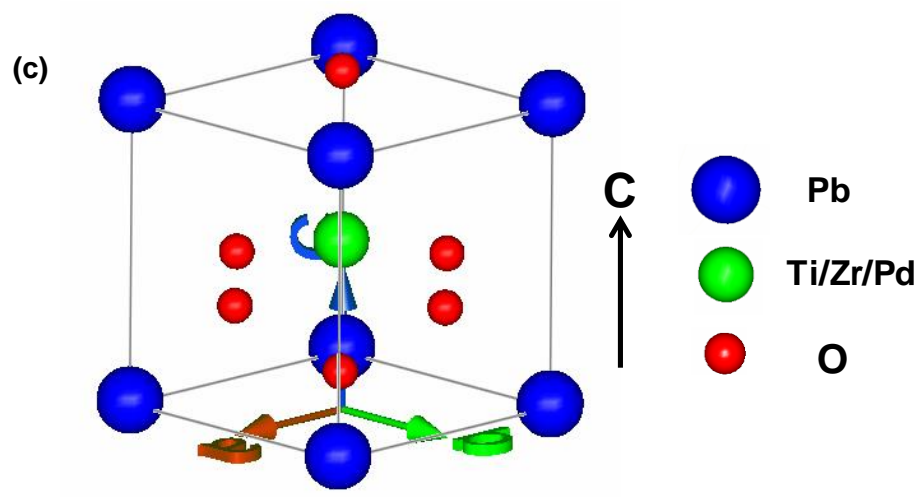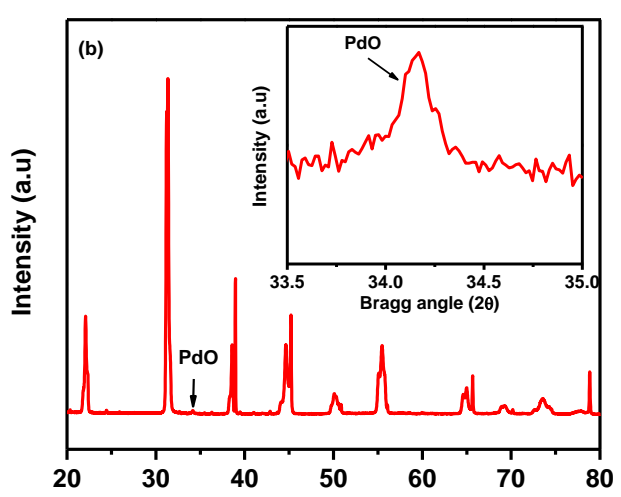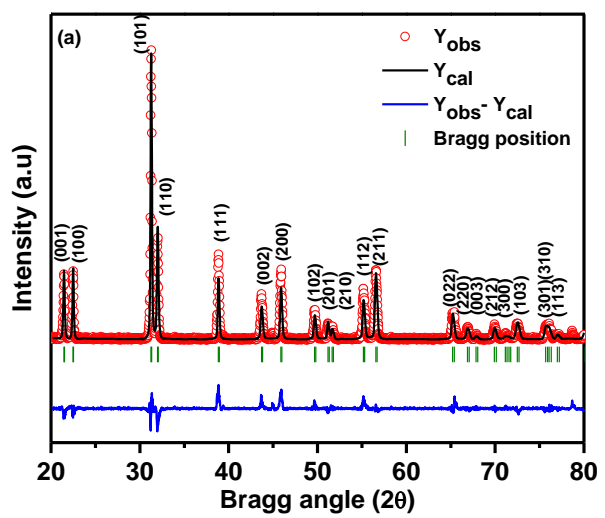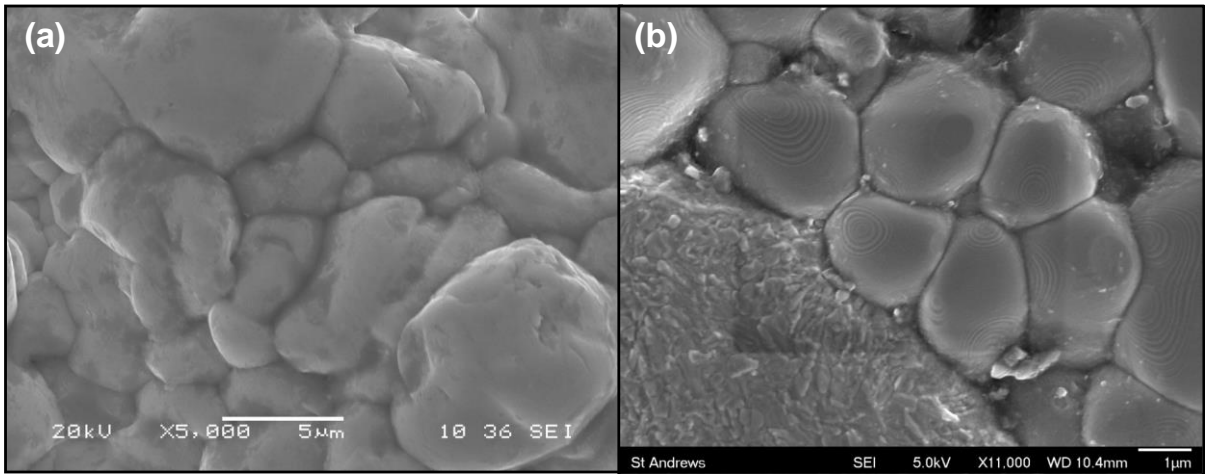
Figure 1. Kumari et al.

(a)

20kV   X5,000   5μm   10 36 SEI

(b)

St Andrews   SEI   5.0kV   X11,000   WD 10.4mm   1μm
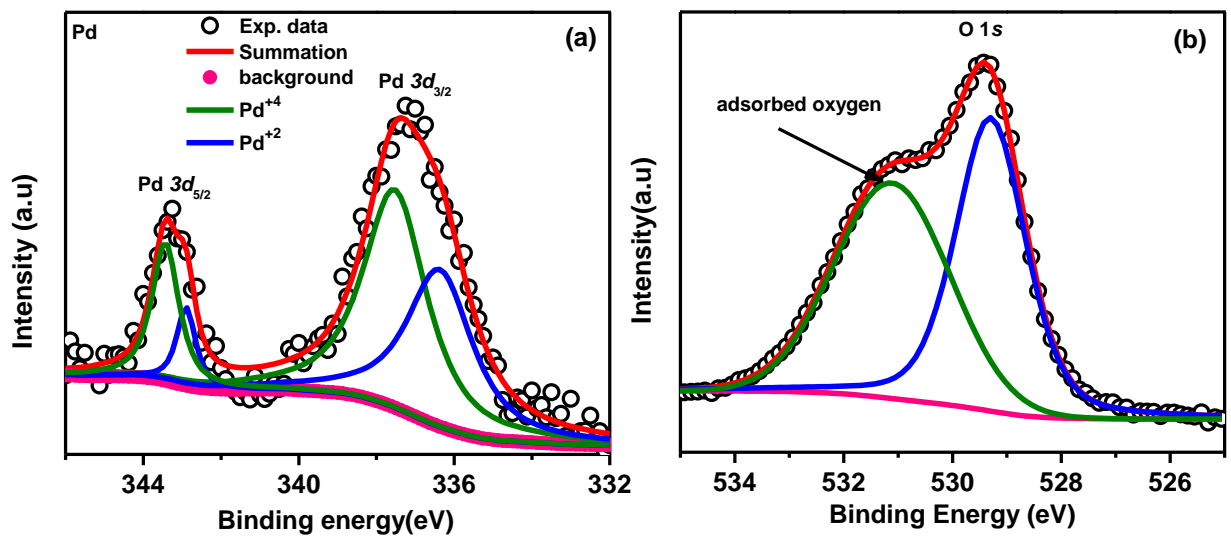
Figure 2. Kumari et al.
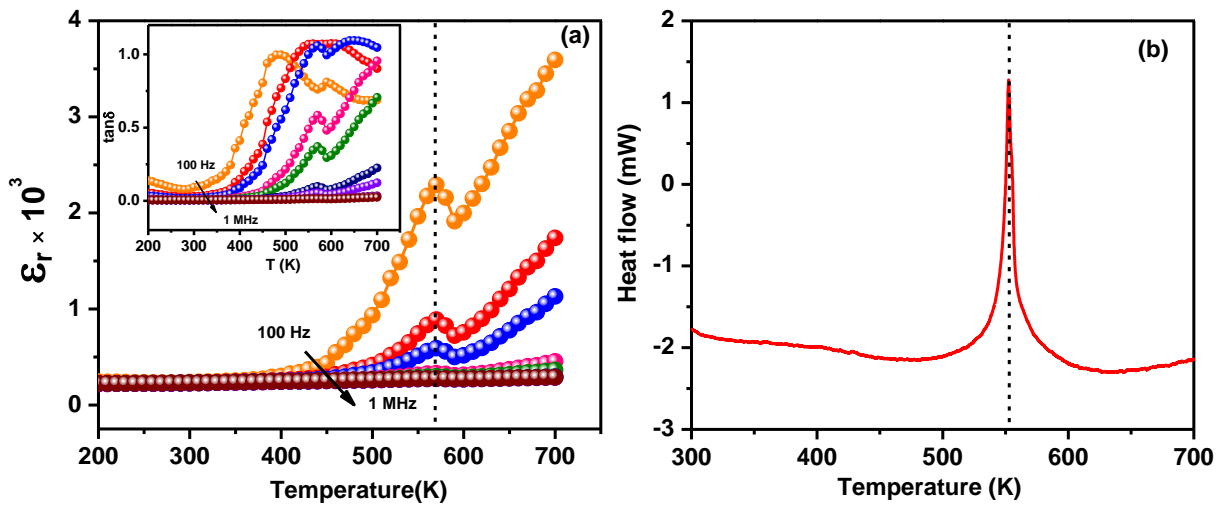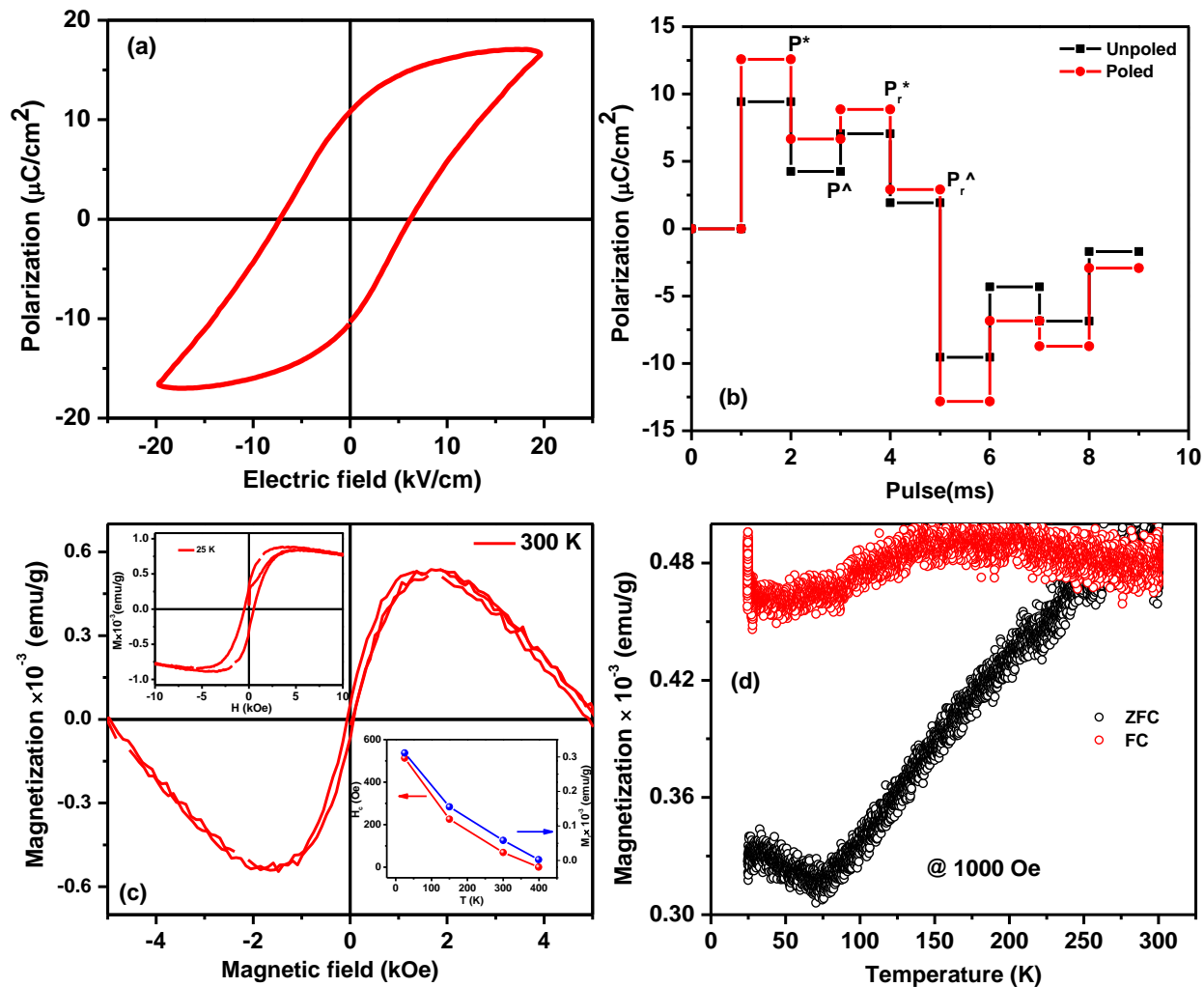
Figure 3. Kumari et al.

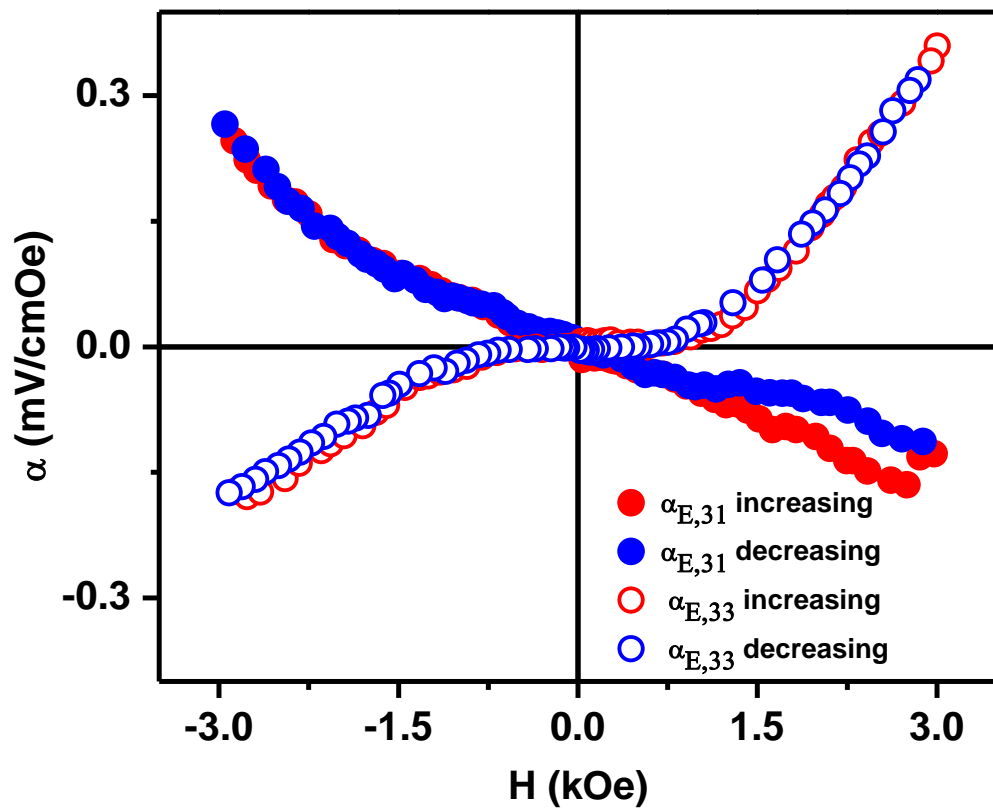**Figure 4. Kumari et al.**

Figure 5. Kumari et al.

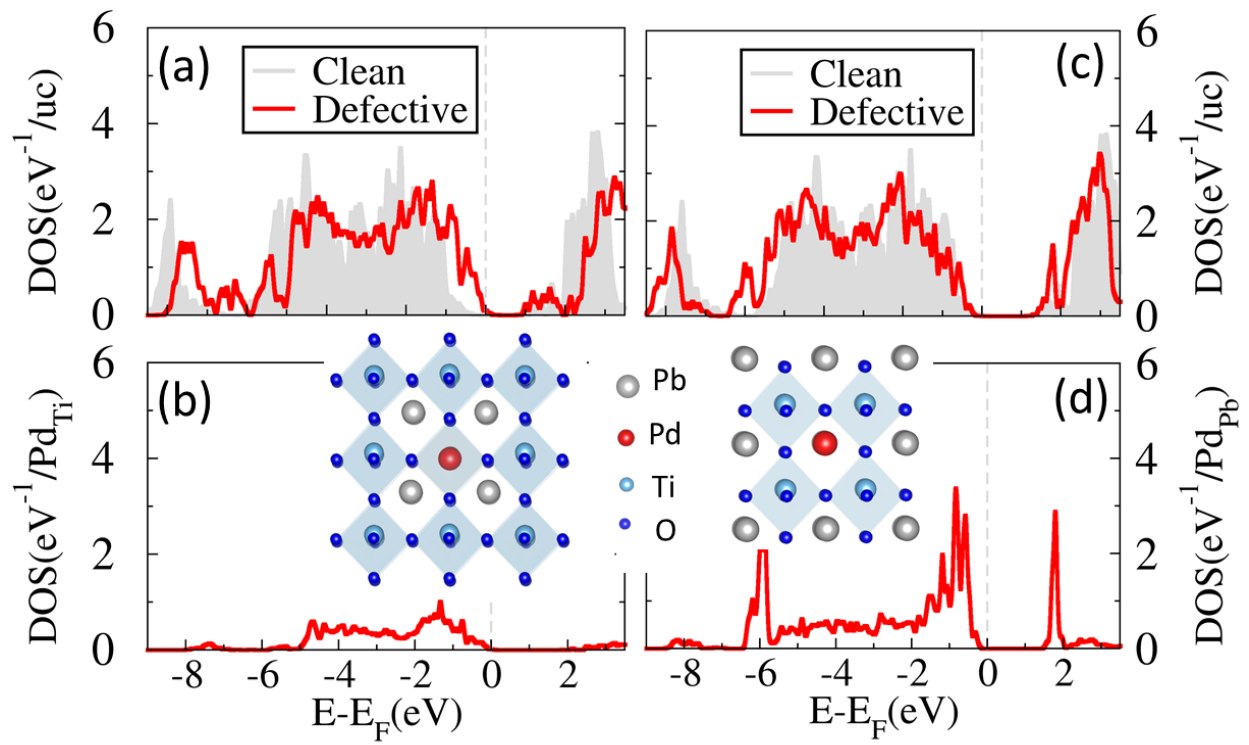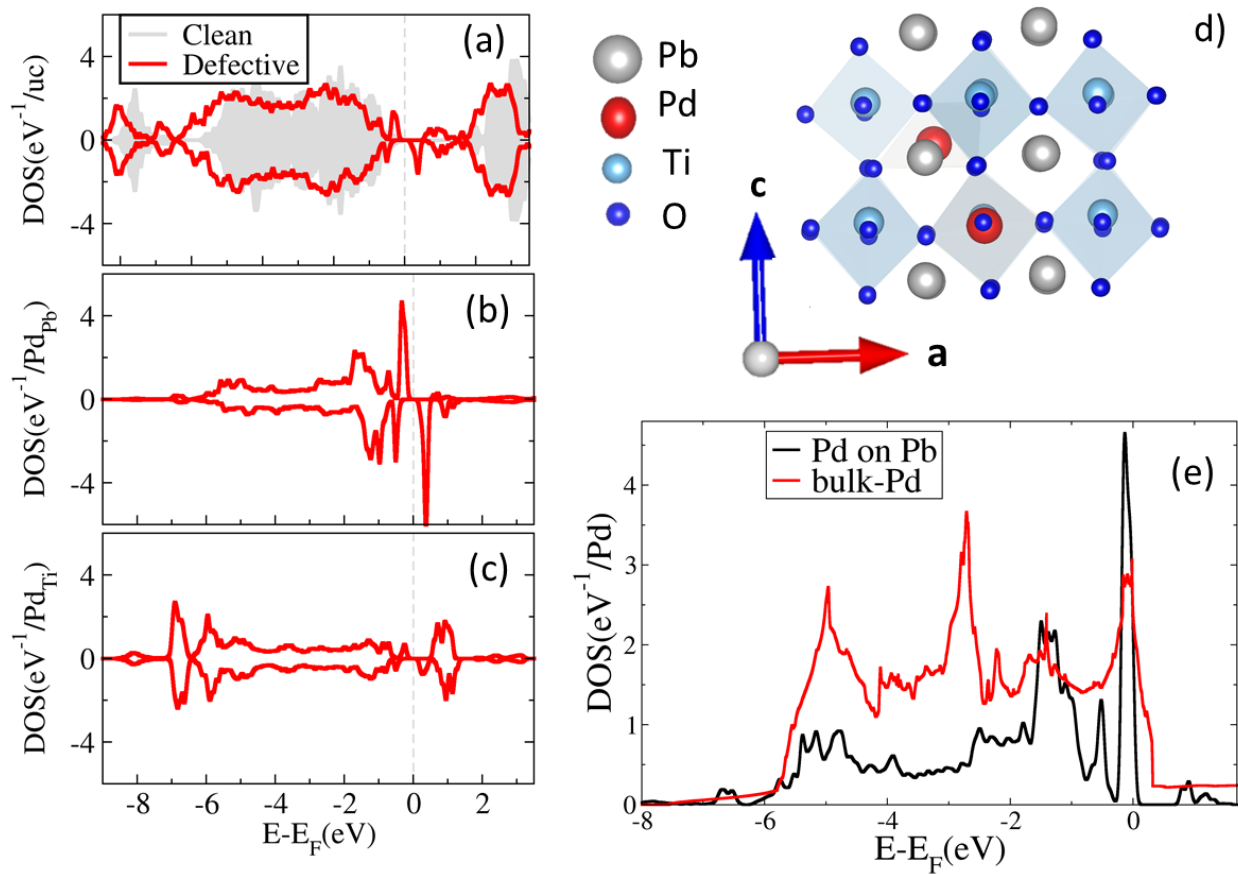**Figure 6. Kumari et al.**

Figure 7. Kumari et al.

Figure 8. Kumari et al.

29

References

[1] W. Eerenstein, N. D. Mathur, J. F. Scott, Nature **442**, 759-765 (2006).

[2] J. F. Scott, Science **315**, 954–959 (2007).

[3] M. Bibes, A. Barthélémy, Nature Mater. **7**, 425–426 (2008).

[4] A. J. Freeman, H. Schmid, *Magnetoelectric Interaction Phenomena in Crystals*, (Gordon and Breach, London, 1975).

[5] Yusuke Tokunaga, Nobuo Furukawa, Hideaki Sakai, Yasujiro Taguchi, Taka-hisa Arima, Yoshinori Tokura, Nature Mater. **8**, 558–562 (2009).

[6] S.-W. Cheong, M. Mostovoy, Nature Mater. **6**, 13–20 (2007).

[7] I. Zutić, J. Fabian, S. Das Sarma, Rev. Mod. Phys. **76**, 323–410 (2004).

[8] T. Kimura, T. Goto, H. Shintani, K. Ishizaka, T. Arima, Y. Tokura, Nature, **426**, 55–58 (2003).

[9] D. A. Sanchez, N. Ortega, A. Kumar, R. S. Katiyar, J. F. Scott, AIP Adv. **1**, 042169 (2011).

[10] D. M. Evans, M. Alex, A. Schilling, A. Kumar, D. Sanchez, N. Ortega, R. S. Katiyar, James Floyd Scott, J. M. Gregg, Adv. Mat. **27**, 6068-6073 (2015).

[11] A. Kumar, I. Rivera, R. S. Katiyar, J. F. Scott, Appl. Phys. Lett. **92**, 132913 (2008).

[12] J. Wang, J. B. Neaton, H. Zheng, V. Nagarajan, S. B. Ogale, B. Liu, D. Viehland, V. Vaithyanathan, D. G. Schlom, U. V. Waghmare, N. A. Spaldin, K. M. Rabe, M. Wuttig, R. Ramesh, Science, **299**, 1719 (2003).

[13] S. Goswami, D. Bhattacharya, L. Keeney, T. Maity, S. D. Kaushik, V. Siruguri, G. C. Das, H. Yang, W. Li, C. Gu, M. E. Pemble, S. Roy, Phys. Rev. B **90**, 104402 (2014).

[14] E. Jartych, T. Pikula, K. Kowal, J. Dzik, P. Guzdek, and D. Czekaj, Nanoscale Res. Lett. **11**, 234 (2016).

[15] A. N. Guthrie, M. J. Copley, Phys. Rev., **38**, 360, (1938).

[16] Aya Obinata, Yuki Hibino, Daichi Hayakawa, Tomohiro Koyama, Kazumoto Miwa, Shimpei Ono, Daichi Chiba, Scientific Reports **5**, 14303 (2015).

[17] M. Birsan, B. Fultz, L. Anthony, Phys. Rev. B, **55**, 11502, (1997).

[18] O. Yamada, F. Ono, I. Nakai, H. Maruyama, K. Ohta, M. Suzuki, Journal of Magnetism and Magnetic Materials, **31-34,** 105-106, (1993).

[19] D. Khomskii, Physics **2**, 20 (2009).

[20] J. F. Scott, NPG Asia Materials, **5** (2013).

[21] N. A. Spaldin, S. W. Cheong, R. Ramesh, Phys. Today **63(10)**, 38 (2010).

[22] Ashok Kumar, Nora Ortega, Sandra Dussan, Shalini Kumari, Dilsom Sanchez, J. F. Scott, Ram S. Katiyar, *Multiferroic Memory: A Disruptive Technology or Future Technology?* (Solid State Phenomena, 189, 2012).

[23] D. K. Pradhan, Venkata S. Puli, Shalini Kumari, Satyaprakash Sahoo, Proloy T. Das, Kallol Pradhan, Dillip K. Pradhan, J. F. Scott, Ram S. Katiyar, The Journal of Physical Chemistry C, **120**, 1936-1944 (2016).

[24] M. Correa, A. Kumar, S. Priya, R. S. Katiyar, J. F. Scott, Phys. Rev. B **83**, 014302 (2011).

[25] A. A. Bokov, S. M. Emelyanov, Physica Status Solidi B **164**, K109–K112, (1991).

[26] Bas B. Van. Aken, Thomas T. M. Palstra, Alessio Filippetti, Nicola A. Spaldin, Nature Materials **3**, 164 - 170 (2004).

[27] R. Saha, A. Sundaresan, C. N. R. Rao, Mater. Horiz. **1**, 20 (2014).

[28] D. Lebeugle, D. Colson, A. Forget, M. Viret, P. Bonville, J. F. Marucco, S. Fusil, Phys. Rev. B. **76**, 024116 (2007).

[29] S. Kumari, N. Ortega, A. Kumar, S. P. Pavunny, J. W. Hubbard, C. Rinaldi, G. Srinivasan, J. F. Scott, Ram S. Katiyar, Journal of Applied Physics **117**, 114102 (2015).

[30] Shalini Kumari, N. Ortega, A. Kumar, R. S. Katiyar, MRS Proceedings, 1636 (2014).

[31] M. Fiebig, J. Phys. D: Appl. Phys. **38**, R123 (2005).

[32] W. Prellier, M. P. Singh, P. Murugavel, J. Phys. Condens. Matter. **17**, R803 (2005).

[33] S. Picozzi, C. Ederer, J. Phys. Condens. Matter. **21**, 303201 (2009).

[34] V. Garcia, M. Bibes, L. Bocher, S. Valencia, F. Kronast, A. Crassous, X. Moya, S Enouz-Vedrenne, A. Gloter, D. Imhoff, C. Deranlot, N. D. Mathur, S. Fusil, K. Bouzehouane, A. Barthélémy, *Science*, **327**, 1106-1110, (2010).

[35] Wenbin Wang, Jun Zhao, Wenbo Wang, Zheng Gai, Nina Balke, Miaofang Chi, Ho Nyung Lee, Wei Tian, Leyi Zhu, Xuemei Cheng, David J. Keavney, Jieyu Yi, Thomas Z. Ward, Paul C. Snijders, Hans M. Christen, Weida Wu, Jian Shen, and Xiaoshan Xu, Phys. Rev. Lett. **110**, 237601 (2013).

[36] Rana Saha, Ajmala Shireen, Sharmila N. Shirodkar, Mukta Shashi Singh, Umesh V. Waghmare, A. Sundaresan, C. N. R. Rao, *Inorg. Chem.* **50**, 9527–9532 (2011).

[37] K. M. Satyalakshmi, M. Alexe, A. Pignolet, N. D. Zakharov, C. Harnagea, S. Senz, D. Hesse, Appl. Phys. Lett., **74**, 603 (1999).

[38] S. Mukherjee, A. Roy, S. Auluck, R. Prasad, R. Gupta, A. Garg, Phys. Rev. Lett. **111**, 087601, (2013).

[39] H. M. Jang, S.-W. Song, K.-S. Lee, Y. S. Son, R. Gupta, A. Garg, J. Ratanapreechachai, J. F. Scott, (npg) Asia Mater. **8**, e42 (2016).

[40] David I. Woodward, Jesper Knudsen, Ian M. Reaney, Phys. Rev. B **72**, 104110 (2005).

[41] Joseph W. Bennett, Ilya Grinberg, Peter K. Davies, Andrew M. Rappe, Phys. Rev. B **82**, 184106 (2010).

[42] G. Srinivasan, E. T. Rasmussen, J. Gallegos, R. Srinivasan, Yu I. Bokhan, V. M. Laletin, Phys. Rev. B **64**, 214408, (2001).

[43] J. Joseph, T. M. Vimala, V. Sivasubramanian, V. R. K. Murthy, Journal of Materials Science, **35,** 1571 – 1575 (2000).

[44] D. Walker, P. A. Thomas, S. P. Collins, Phys. Status Solidi A **206**, 1799 (2009).

[45] H. M. Song, J. I. Zink, N. M. Khashab, Chem. Mater. **27**, 29 (2015).

[46]Alexandre Baylet, Patrice Mare´cot, Daniel Duprez, Paola Castellazzi, Gianpiero Groppi, Pio Forzatti, Phys. Chem. Chem. Phys., **13**, 4607–4613 (2011).

[47] O. Madelung, U. Rössler, M. Schulz, *PdO: magnetic properties* (Landolt-Börnstein - Group III Condensed Matter 41D, Springer-Verlag Berlin Heidelberg 2000).

[48] Shalini Kumari, Nora Ortega, Dhiren K. Pradhan, Ashok Kumar, J. F. Scott, Ram S. Katiyar, Journal of Applied Physics **118**, 184103 (2015).

[49] Shalini Kumari, Nora Ortega, Ashok Kumar, J. F. Scott, R. S. Katiyar, AIP Advances **4**, 037101 (2014).

[50] Lidiya S. Kibis, Andrey I. Stadnichenko, Sergei V. Koscheev, Vladimir I. Zaikovskii, Andrei I. Boronin, J. Phys. Chem. C, **116**, 19342−19348 (2012).

[51] J. -N. Kim, K. -S. Shin, D. -H. Kim, B. -O. Park, N. -K. Kim, S. -H. Cho, Appl. Surf. Sci. **206**, 119 (2003).

[52] C. D. Wagner, W. M. Riggs, L. E. Davis, J. F. Moulder, G. E. Muilenberg, *Handbook of X-ray Photoelectron Spectroscopy* (Perkin-Elmer Corp., Physical Electronics Division, Eden Prairie, MN, 1979).

[53] J. He, X. Lu, W. Zhu, Y. Hou, R. Ti, F. Huang, X. Lu, T. Xu, J. Su, *J.* Zhu, Appl. Phys. Lett. **107**, 012409 (2015).

[54] G. H. Khorrami, A. K. Zak, S. M. Banihashemian, Advanced Powder Technology **25** 1319–1324 (2014).

[55] G. Arya, R. K. Kotnala, N. S. Negi, J. Am. Ceram. Soc. **97**, 1475 (2014).

[56] G. Harshe, J. P. Dougherty, R. E. Newnham, Int. J. Appl. Electromag. Mater. **4**, 145 (1993).

[57] M. Avellaneda, G. Harshe, J. Intell. Mater. Sys. Struc. **5**, 501 (1994).

[58] G. Srinivasan, E. T. Rasmussen, J. Gallegos, R. Srinivasan, Yu. I. Bokhan, V. M. Laletin, Phys. Rev. B **64**, 214408 (2001).

[59] V. M. Laletin, G. Srinivasan, Ferroelectrics **280**, 177 (2002).

[60] E. C. Stoner, Proc. R. Soc. London, Ser. A **165**, 372 (1938).

[61] P. E. Blöchl, Phys. Rev. B **50**, 17953 (1994).

[62] G. Kresse, D. Joubert, Phys. Rev. B **59**, 1758 (1999).

[63] G. Kresse, J. Furthmuller, Phys. Rev. B **54**, 11169 (1996).

[64] J. Neugebauer, M. Scheffler, Phys. Rev. B **46**, 16067 (1992).

[65] W. Yi, Y. Matsushita, M. Tanaka, A. A. Belik, Inorg. Chem. **51**, 7650 (2012).